Earth, Planets and Space

EXPRESS LETTER

Open Access

Resistivity characterisation of Hakone volcano, Central Japan, by three-dimensional magnetotelluric inversion

Ryokei Yoshimura[1*], Yasuo Ogawa[2], Yohei Yukutake[3], Wataru Kanda[2], Shogo Komori[4,5], Hideaki Hase[2,6], Tada-nori Goto[7], Ryou Honda[3], Masatake Harada[3], Tomoya Yamazaki[1], Masato Kamo[1], Shingo Kawasaki[1], Tetsuya Higa[8], Takeshi Suzuki[8], Yojiro Yasuda[9], Masanori Tani[7] and Yoshiya Usui[2]

Abstract

On 29 June 2015, a small phreatic eruption occurred at Hakone volcano, Central Japan, forming several vents in the Owakudani geothermal area on the northern slope of the central cones. Intense earthquake swarm activity and geodetic signals corresponding to the 2015 eruption were also observed within the Hakone caldera. To complement these observations and to characterise the shallow resistivity structure of Hakone caldera, we carried out a three-dimensional inversion of magnetotelluric measurement data acquired at 64 sites across the region. We utilised an unstructured tetrahedral mesh for the inversion code of the edge-based finite element method to account for the steep topography of the region during the inversion process. The main features of the best-fit three-dimensional model are a bell-shaped conductor, the bottom of which shows good agreement with the upper limit of seismicity, beneath the central cones and the Owakudani geothermal area, and several buried bowl-shaped conductive zones beneath the Gora and Kojiri areas. We infer that the main bell-shaped conductor represents a hydrothermally altered zone that acts as a cap or seal to resist the upwelling of volcanic fluids. Enhanced volcanic activity may cause volcanic fluids to pass through the resistive body surrounded by the altered zone and thus promote brittle failure within the resistive body. The overlapping locations of the bowl-shaped conductors, the buried caldera structures and the presence of sodium-chloride-rich hot springs indicate that the conductors represent porous media saturated by high-salinity hot spring waters. The linear clusters of earthquake swarms beneath the Kojiri area may indicate several weak zones that formed due to these structural contrasts.

Keywords: Hakone volcano, Magnetotellurics, Resistivity structure, Three-dimensional inversion

Introduction

Hakone volcano is located at the northern end of the Izu–Mariana volcanic arc in Central Japan, 100 km west of Tokyo (index map in Fig. 1a). On 29 June 2015, a small phreatic eruption was observed in the Owakudani geothermal area, which is located on the northern slope of the central cones of Hakone volcano, forming several vents, although there is no prior historical record of magmatic eruptions there. However, long-term fumarolic activity has been observed across this geothermal area. Ahead of these phreatic events (from the end of April 2015), the seismicity had increased around the central cones (Fig. 1a; after Yukutake et al. 2017), with several distinct geodetic signals. Inside Hakone caldera, several similar earthquake swarm activities have occurred without an associated eruptive event. These swarm activities were detected by a modern seismic network, which has captured the distribution of earthquake hypocentres for swarm activities in 2001, 2006, 2009 and 2013 (e.g. Yukutake et al. 2010, 2011, 2015; the epicentral distributions of some of these swarms are plotted in Additional file 1: Fig. S1). Such swarm activities could be summarised as being predominantly beneath the central cones

*Correspondence: ryokei@eqh.dpri.kyoto-u.ac.jp
[1] Disaster Prevention Research Institute, Kyoto University, Gokasyo, Uji, Kyoto 611-0011, Japan
Full list of author information is available at the end of the article

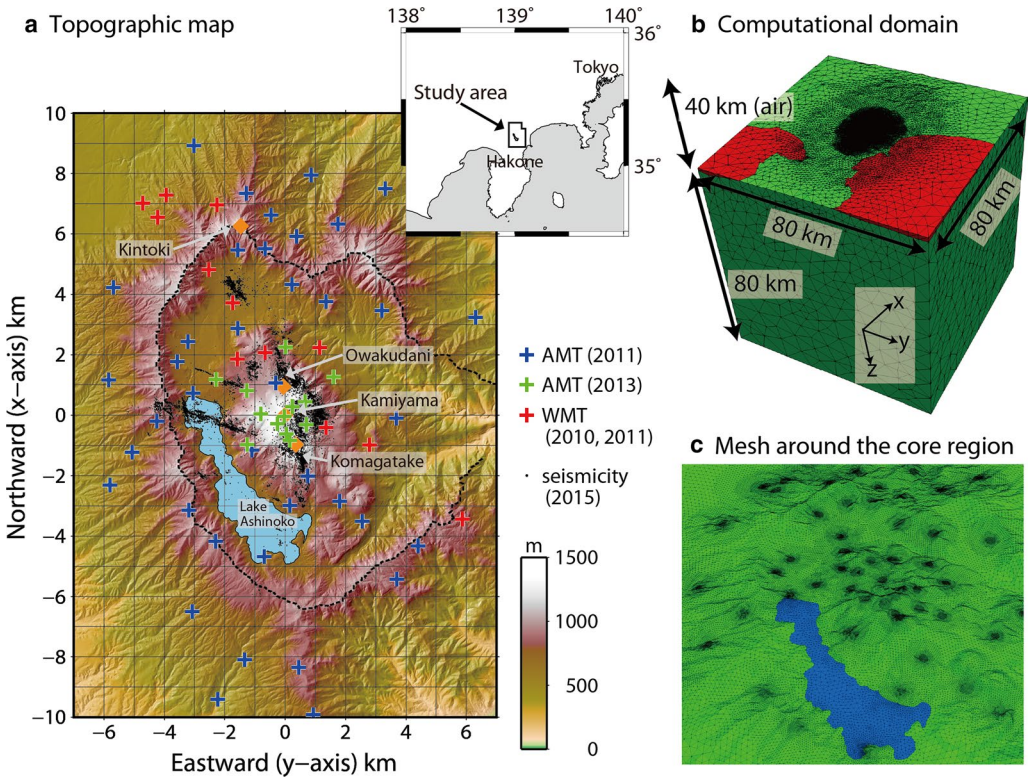

Fig. 1 Topographic map of the study area and computational mesh used in the three-dimensional resistivity inversion. **a** Topographic map of Hakone volcano, Central Japan, highlighting the spatial distribution of the magnetotelluric observation sites used in this study. The blue, green and red plus symbols indicate the 2011 AMT observations, the 2013 AMT observations and the 2010 and 2011 WMT observations, respectively. The topography was extracted from a 10-m DEM provided by the Geospatial Information Authority of Japan. The epicentres of the earthquake swarms from April to October 2015, as determined by Yukutake et al. (2017), are plotted as black dots. The black dotted line indicates the caldera rim of Hakone volcano. The orange diamonds mark the Owakudani geothermal area, central cones (Mts. Kamiyama and Komagatake) and Mt. Kintoki. The surface extent of Lake Ashinoko is shown in blue. **b** Subsurface computational domain without air elements. The origin of the mesh was set at the sea level just beneath Mt. Kamiyama. The tetrahedral lattice in the central portion of the computational domain, covering the core region of Hakone volcano and encompassing all the MT/AMT sites, was made at a finer resolution. The green, red and blue colours indicate the elements located in land, seawater and lake water, respectively. **c** Surface mesh around the core region. The tetrahedral lattice was subdivided into an even finer mesh around the AMT/WMT sites

and partially beneath nearby areas, namely the Kojiri area (located at the northern end of Lake Ashinoko) and the southern extent of Mt. Kintoki (located at the northern part of the caldera rim), although the 2009 swarm activity was only detected beneath the Kojiri area. These earthquake swarms, which occurred beneath the Kojiri area and nearby Mt. Kintoki, showed clear planar distributions (e.g. Yukutake et al. 2010, 2011). In addition, immediately after the occurrence of the 2011 great Tohoku Earthquake, seismicity inside the caldera was remotely triggered (Yukutake et al. 2013), with an earthquake distribution that included areas of previously low seismicity, as well as the frequent swarms mentioned above (see Additional file 1: Fig. S1). Although the geophysical properties around the individual seismogenic zones of the above-mentioned swarm activities have improved our understanding of the 2015 eruption and the other activities, little is known about the shallow structure beneath Hakone caldera.

The purpose of this study is to map the three-dimensional electrical resistivity structure, discuss the volcanic system and characterise the structure of Hakone caldera. Since resistivity is sensitive to temperature (including thermal alteration) and the presence of fluids, it is commonly applied to infer the structural setting in volcanic and geothermal environments (e.g. Nurhasan et al. 2006; Kanda et al. 2008; Komori et al. 2013; Yamaya et al. 2013; Gasperikova et al. 2015; Seki et al. 2015, 2016; Usui et al. 2017). In our study area, we obtained magnetotelluric (MT) data in the dense site array (Ogawa et al. 2011; Yoshimura et al. 2012, 2013) to infer the structure of Hakone volcano, with a focus on shallow caldera

structures. The topographic effects due to the relief of Hakone volcano within the survey area are accounted for in the inversion by applying the code developed by Usui (2015), which treats the model as a series of unstructured tetrahedral elements, to achieve a realistic representation of surface topography and subsurface resistivity structures.

Magnetotelluric data

We conducted the audio-frequency magnetotelluric (AMT; 0.35–10,400 Hz) surveys at 39 sites, covering the whole of Hakone caldera, in December 2011 (Fig. 1a). We also acquired complementary AMT measurements at 15 sites (including remeasurement sites; Fig. 1a) around the summit area of the central cones (Mts. Kamiyama and Komagatake) in April 2013. We calculated the MT responses using only nighttime data (00:00–04:00 local time) to avoid artificial noise due to electrical power lines, buildings and leakage currents from DC electric railways. Furthermore, we applied the remote reference technique (Gamble et al. 1979) to further reduce the noise, where we selected a simultaneous operation site for each MT measurement location within the study area as a reference. This 'mutual' referencing approach was undertaken within the survey area because we did not have a dedicated reference site during our AMT campaigns, which resulted in many 'reference' sites (the maximum, minimum and average distances to each reference are 14.3, 1.8 and 7.5 km, respectively). We also included wideband magnetotelluric (WMT) data from 12 sites (Fig. 1a) that were previously acquired across the study area. Although WMT data have the potential to estimate the MT responses from 320 Hz to 3000 s, the longer response periods (< 0.35 Hz) were too noisy in this field, even after careful treatments for noise reduction. The MTU-5A and MTU-5 systems (Phoenix Geophysics) were used to acquire the electromagnetic data for the AMT and MT surveys. The details of these AMT and WMT campaigns were reported by Ogawa et al. (2011), Yoshimura et al. (2012) and Yoshimura et al. (2013). Figure 1a shows the distribution of the sites used in this study, comprising 52 AMT sites and 12 WMT sites. We utilised 20 frequencies, ranging from 0.43 to 320 Hz, for the three-dimensional inversion of all 64 sites, since the frequency range of AMT and WMT surveys overlaps from 0.35 to 320 Hz, and the penetration depth of the higher parts of the AMT responses (> 320 Hz) is too shallow to be dealt with in the present computational mesh. After manual inspection of data to remove all observations that exhibited large errors and artificial jumps, 8904 data observations (real and imaginary parts of the responses) were selected for the inversion.

Three-dimensional inversion and modelled resistivity structure

We inverted the full components of the impedance tensors by applying the code developed by Usui (2015). This inversion code employs the edge-based finite element method, which uses unstructured tetrahedral elements to incorporate the actual topography into a computational mesh, and then estimates the subsurface resistivity structure and the distortion tensor of each site. If the standard deviation of the data was less than 5% of the largest value of the off-diagonal components (error floor), it was forced to be the error floor value to avoid over-fitting.

We set the computational domain as a 80 km × 80 km × 120 km (including a 40-km air layer) mesh, with the origin of the mesh set at the sea level, just beneath Mt. Kamiyama. We gave special consideration to three inner surfaces within this computational domain, namely the solid surfaces (land surface, seafloor surface and bottom of Lake Ashinoko), the seawater surface and the surface of Lake Ashinoko. During the mesh generation, we first discretised the flat surface and preserved the lakefront and coast, following the Delaunay triangulation algorithm. Here, the discretised triangles were created at a higher density towards the origin of the domain and the locations of MT observation sites. The nodes corresponding to the seafloor and lake were then duplicated and preserved along the Z-axis in reference to the actual depth information. This actual depth information was taken from the 250-m-bathymetric-mesh data (Kisimoto 2000) and digitised from map image of the Geospatial Information Authority of Japan (GSI). The nodes that should be located above sea level (ASL) were then shifted upward along the Z-axis and adjusted according to the 10-m digital elevation model produced by GSI. The outer surfaces of the computational domain (top, bottom and sides) were also discretised to triangles. The final three-dimensional mesh was generated using the TetGen mesh generator (Si 2015), with the produced mesh shown in Fig. 1b, c. The mesh in the central portion of the domain, which includes Hakone volcano and the MT site locations, is finer, as mentioned above. We call the central finer portion, ranging from − 10 to 10 km in the x-direction, − 7 to 7 km in the y-direction and 5 km to the solid surface in the z-direction, the core region. The total number of nodes and elements in this mesh is 222,716 and 1,359,179, respectively. The elements, excluding those located in the air and water regions of the mesh, were grouped into 27,547 parameter cells, which defined our unknown model parameters, following the algorithm described by Usui (2015).

In the initial model, the resistivity values were set to 100 Ωm for land, 0.25 Ωm for seawater, 137 Ωm for lake water, which is the measured value of Hirano et al. (1982),

and 10^9 Ωm for air. The resistivity value of each element that was situated in sea, lake and air was fixed during the iterations. The inversion code seeks the model vector that minimises the objective function, which is a weighted sum of the data misfit, model roughness and strength of the galvanic distortion. The trade-off parameters α^2 and β^2 are constant factors of the model roughness and the strength of the galvanic distortion, respectively. Here, we used a fixed value of $\beta^2 = 0.01$ since several reports had demonstrated that such a small trade-off parameter was sufficient for the MT inversion (e.g. Sasaki and Meju 2006; Avdeeva et al. 2015; Usui et al. 2017). However, we ran six inversions with various values of α^2 (100, 31.6, 10, 3.16, 1.0 and 0.316) and determined the performance of each model in terms of both its fit to the various parts of the dataset and the differences with the other models. We chose $\alpha^2 = 1.0$ as the preferred trade-off parameter based on this analysis. After 14 iterations, the objective function changed by less than 1% of the previous iteration value, yielding our best-fit model to the MT observations, with an RMS (root-mean-square) misfit that decreased from 52.14 (initial model) to 4.95 (final model: iteration 14). Figure 2 compares the apparent resistivity and phase maps of the observed data and the calculated responses from the best model. The apparent resistivity and phase were calculated from the sum of the squared elements' invariant impedance (Szarka and Menvielle 1997). There is a good agreement between observed and calculated responses.

To evaluate the sensitivity of the best model, we analysed the absolute sensitivity and sensitivity density distributions. The absolute sensitivity (AS) was defined by Usui (2015) as $s_i = \sum_j^{N_d} \left| \frac{1}{\sigma_j} \frac{\partial d_j}{\partial \log \rho_i} \right|$, where d_j, σ_j and ρ_i denote the jth data observation, the standard deviation of the jth data observation and the log-resistivity of the ith parameter cell, respectively. The absolute sensitivity is essentially the summation of each column of the sensitivity (Jacobian) matrix. To reduce the bias due to large elements, Schwalenberg et al. (2002) divided AS by the volume of the respective element, and we call the resulting sums the absolute sensitivity density (ASD). The AS and ASD histograms are shown in Fig. 3, which reveals characteristic distributions, with a trend change at $10^{1.2}$ in the AS histogram and a bimodal distribution whose two peaks are sectioned at $10^{-7.5}$ in the ASD histogram. Most of the elements inside the core region (grey columns in Fig. 3) have a relatively high sensitivity. We thus defined the lower limits of the acceptable sensitivity as $10^{1.2}$ in AS and $10^{-7.5}$ in ASD. All elements above these sensitivity limits were visualised in the results as sensitive and considerable parts.

Figure 4 shows vertical cross sections through the best-fit three-dimensional resistivity model along several N–S and E–W profiles. The locations of the cross sections are denoted at the top of each panel according to the coordinate grid shown in Fig. 1a. Several horizontal slices of the resistivity structure are also shown in Fig. 5, with the sea level altitude denoted at the top of each panel. Four clearly defined conductors are present in the final model. One is a bell-shaped structure that is located just beneath the central cones. Two conductors exist either near the bell-shaped conductor or laterally protrude from its base. The fourth conductor is located beneath the northern edge of the caldera. We discuss the implications of these four conductors in the following section. While we recognise that there are also several small conductive patches in the outer part of the core region, these four conductors meet our current goal of characterising the shallow structure beneath Hakone caldera and are thus the focus of our discussion and interpretation.

Discussion and conclusions

We first compare our model with the two-dimensional NW–SE image proposed by Ogawa et al. (2011). It is clear that the two results share certain similarities in a broad sense, particularly the observation of the conductor beneath the northern end of the Hakone caldera that dips to the northwest, which is further supported by the seismic velocity structure of the region (Yukutake et al. 2015). However, in the central part of our study area, which corresponds to the southern end of the Ogawa et al. (2011) profile, a significant and previously unidentified feature was discovered inside the caldera in our model, because the dense array data of the present study enabled us to resolve the fine and lateral heterogeneous electrical structure there.

We then interpreted the major above-mentioned conductors that were identified in our model based on the nature of the modelled resistivity anomalies and the results of previous studies. A significant conductor (< 10 Ωm) was detected beneath the central cones (Mts. Kamiyama and Komagatake). This conductor has a cap-like shape in vertical section (e.g. Fig. 4b, c, f) and a doughnut shape in horizontal section (e.g. Fig. 5b), thus possessing a stereoscopic bell shape. This bell-shaped conductor surrounds a relatively resistive body (10–100 Ωm). Such a bell-shaped conductor beneath the central cone or geothermal/fumarolic area has been previously detected at other volcanoes (e.g. Nurhasan et al. 2006; Kanda et al. 2008; Komori et al. 2013; Yamaya et al. 2013; Usui et al. 2017). With reference to the conceptual model of a geothermal system described by Pellerin et al. (1996), we interpret that the bell-shaped conductor and the resistive body represent an impermeable layer consisting of altered clays and a bounded hydrothermal reservoir, respectively. Ohba et al. (2011) reported a temperature of

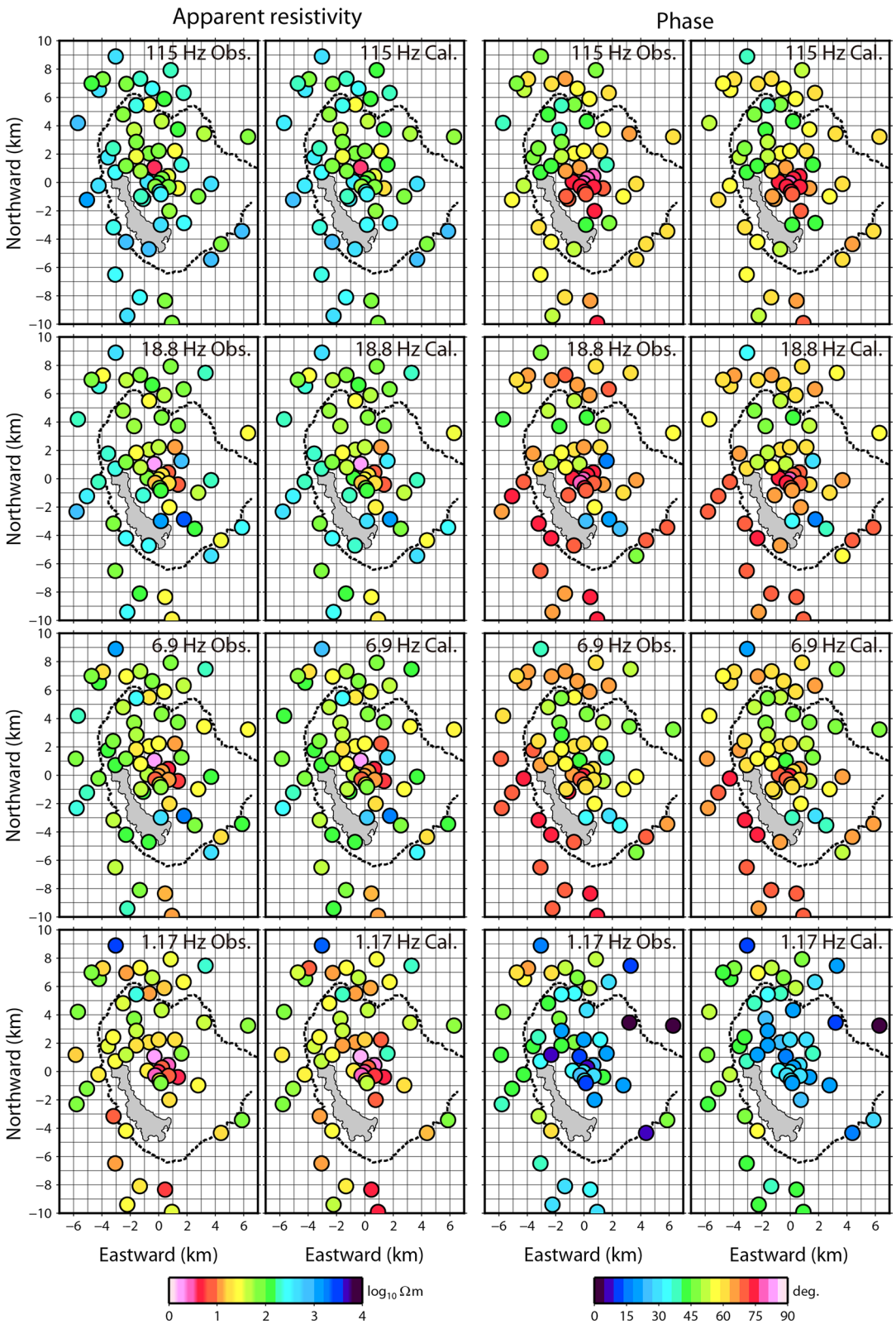

Fig. 2 Apparent resistivity and phase maps for the observed data (Obs.) and calculated responses (Cal.) from the best-fit resistivity model (Figs. 4, 5) for four frequencies (1.17, 6.9, 18.8 and 115 Hz). The responses shown here were calculated from the sum of the squared elements' invariant impedances. See the text for more details. The dotted line indicates the caldera rim, and the shaded region marks the surface extent of Lake Ashinoko

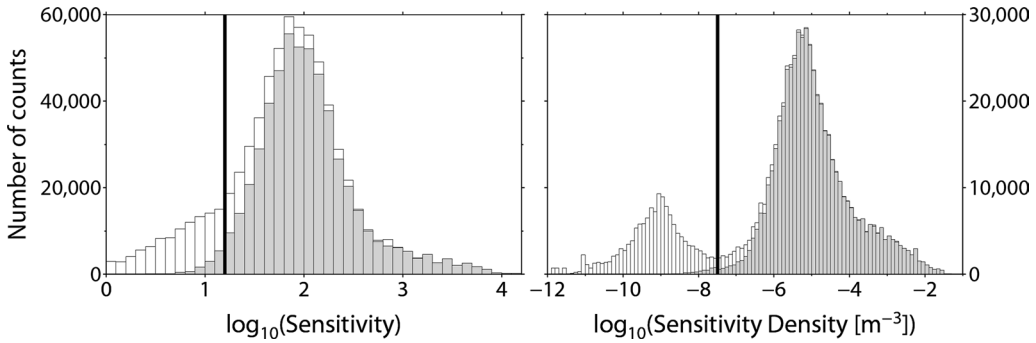

Fig. 3 Histograms of the absolute sensitivities (left panel) and absolute sensitivity densities (right panel) for the core region (grey) and exterior (white). The bins cover 0.1 intervals. The sensitivity density is divided by the volume of the corresponding element to avoid biasing from large elements. The setup criteria ($10^{1.2}$ in absolute sensitivity and $10^{-7.5}$ in sensitivity density) of the lower limit of relatively high-sensitive elements are indicated by thick lines

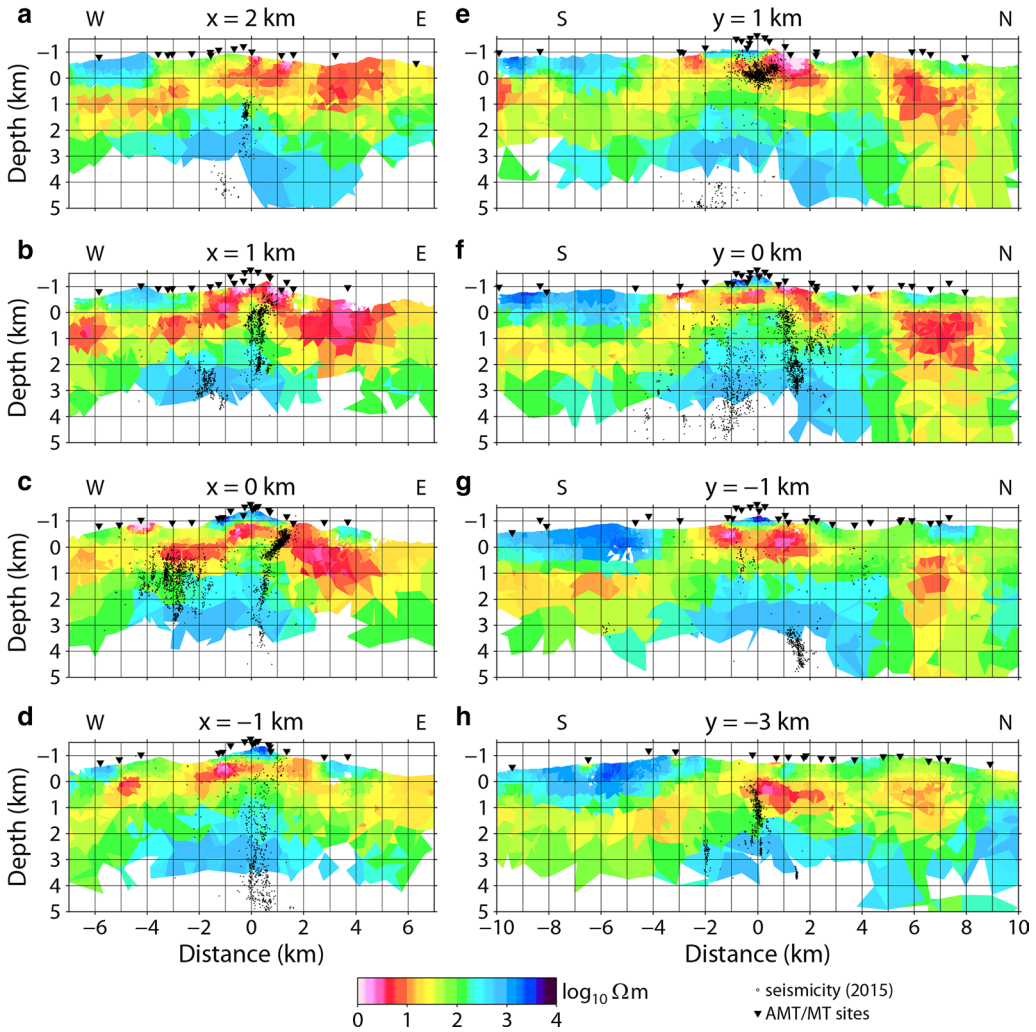

Fig. 4 Vertical cross sections of the three-dimensional resistivity structure. Only the elements for which the model results exceeded the sensitivity and sensitivity density criteria (vertical black lines in Fig. 3) are plotted. Only the subsurface elements are shown here. **a**–**d** cross the study area in the E–W direction at $x = 2$, 1, 0 and − 1 km, respectively. **e**–**h** cross the study area in the N–S direction at $y = 1$, 0, − 1 and − 3 km, respectively. The inverted black triangles indicate the AMT/MT measurement sites located within ± 1.5 km of each profile. The earthquake hypocentres determined by Yukutake et al. (2017) that occurred within ± 0.25 km of each profile are also plotted as black dots. See Fig. 1 for the profile locations, AMT/WMT sites and earthquake hypocentres

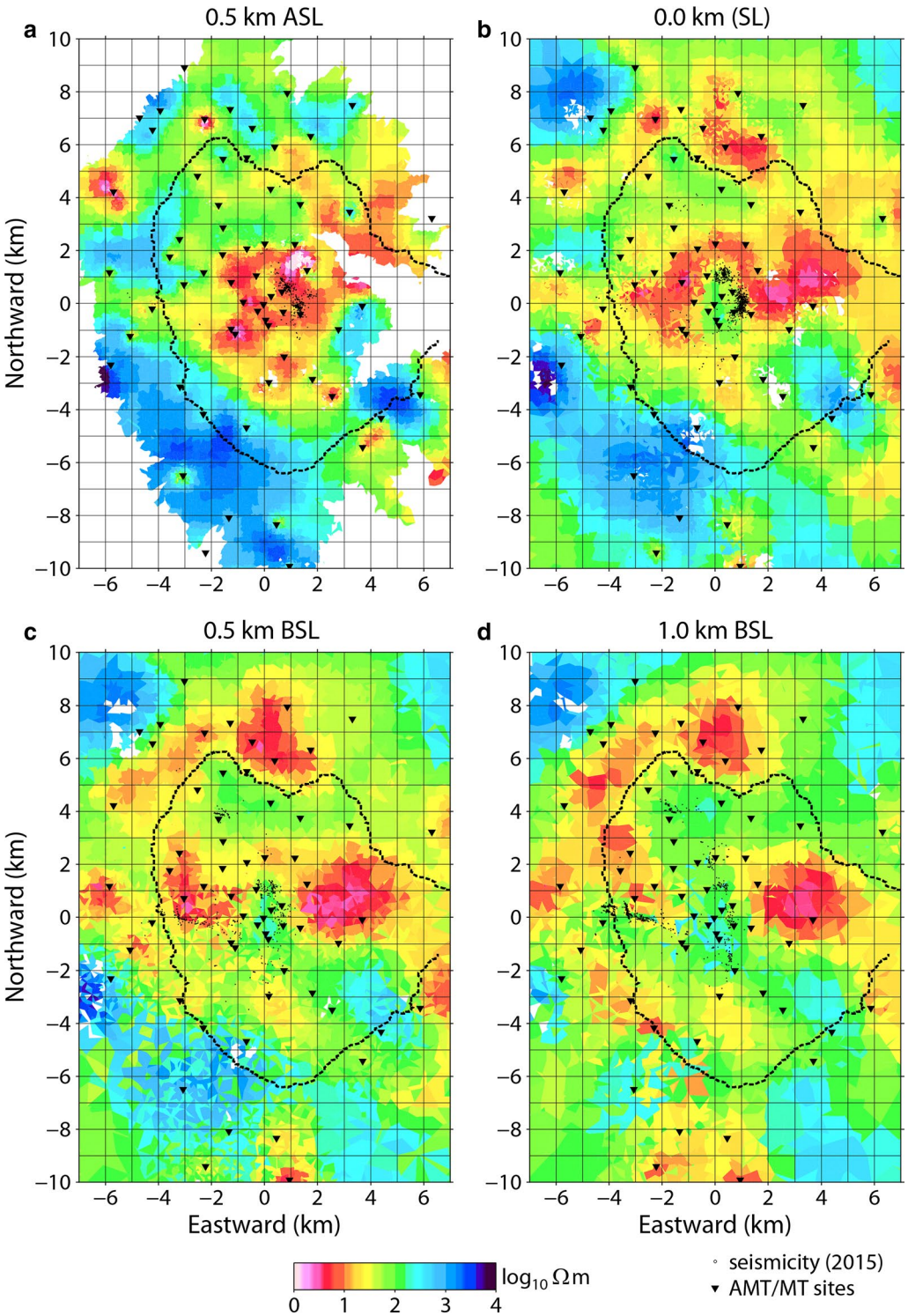

Fig. 5 Horizontal slices of the three-dimensional resistivity structure for various depths. Visualised elements are selected in the same manner as in Fig. 4. **a**–**d** show the XY planes at $z = -0.5$ km (0.5 km above sea level: ASL), $z = 0.0$ km (sea level: SL), $z = 0.5$ km (0.5 km below sea level: BSL) and $z = 1.0$ km (1.0 km BSL), respectively. Inverted black triangles represent the locations of the AMT/WMT sites. The earthquake epicentres that occurred within ± 0.125 km of the cutting-plane are shown as black dots. The present caldera rim of Hakone volcano is indicated by the dotted black line

260 °C at the bottom of a borehole (500 m depth) in the Owakudani geothermal area, which corresponds to the top of the resistive body inside the bell-shaped conductor, where $x=1$, $y=0$ and $z=-0.5$ km (0.5 km ASL) in our coordinate system. This temperature estimation supports our interpretation, because the smectite-rich zone or the transition zone from smectite to illite/chlorite generally occurs in the 100–250 °C temperature range and possesses both a low resistivity and a low permeability (e.g. Ussher et al. 2000; Gasperikova et al. 2015). Comparison of this resistivity structure with the distribution of earthquake swarms in the region (Yukutake et al. 2017) highlights the good agreement between the upper limit of seismicity beneath the central cones and the bottom of the low-resistivity bell-shaped conductor (Fig. 4b, c, f). While considerable seismic activity occurred below this conductor (namely inside the relatively high-resistivity body), there were few earthquakes within the conductive body, which supports the presence of a hydrothermally altered zone here. Furthermore, the fact that most of the earthquakes were located in the relatively high-resistivity body suggests that this body consists of brittle rock at temperatures below 400 °C. Enhanced volcanic activity (e.g. increasing heat supply from the deeper part) may cause the volcanic fluids to flow through the resistive body and promote brittle failure of the structure. It is highly probable that the shallower overlying bell-shaped conductor plays the important role of acting as a cap or seal that restricts the upwelling of volcanic fluids. Thus, several observations that target the base of the bell-shaped conductor can help us understand the evolution of Hakone volcanism, particularly the stage of preparation for phreatic eruptions.

Other significant structural aspects within the caldera region are two large buried conductors: one beneath the Gora area ($x=1$, $y=3$ km in Figs. 1, 5) and the other beneath the Kojiri area ($x=1$, $y=-3$ km in Figs. 1, 5), which either exists near the bell-shaped conductor or laterally protrudes from its base. The conductor located beneath the Gora area broadens and deepens, possessing a bowl-like or funnel-like shape. Mannen (2014) reported a buried caldera structure around the Gora area that was filled by lacustrine sediments and porous tuffaceous rock, as evidenced by geological surveys, borehole explorations and a gravity anomaly analysis. Mannen (personal communication) suggests that three more small buried calderas (including the Kojiri area) occur within the present Hakone caldera. Furthermore, there are many hot springs in the Gora area, whose high-temperature waters possess high concentrations of sodium chloride. These lines of evidence lead us to interpret the large conductors beneath the Gora and Kojiri areas as porous media saturated by high-salinity hot spring waters.

Earthquake swarm activity in the Kojiri area provides additional insights into the structural significance of this buried conductor and its immediate surrounds. Several linear clusters of swarms have been observed in the Kojiri area between 2001 and 2015, surrounding the bowl-shaped conductor (Fig. 4b, h, and Additional file 1: Figs. S2b and S2d), whereas few earthquakes have been recorded in the Gora area. Furthermore, the seismicity beneath the southern extent of Mt. Kintoki, which was possibly remotely triggered by the 2011 great Tohoku earthquake (Additional file 1: Fig. S1), was also observed along the edge of the buried conductor in this area (Additional file 1: Fig. S2c, 5 km north of the origin). Yukutake et al. (2011) suggested that the earthquake swarms observed around the Kojiri area in 2009 were activated by fluid flow along thin plane-like zones. The earthquake swarm beneath the southern extent of Mt. Kintoki also showed clear linear alignments (Yukutake et al. 2010). Since the bowl-shaped conductor beneath the Kojiri area is likely indicative of a buried structure containing saturated fluids, a series of weak zones may have evolved along the outer boundary of this structural resistivity contrast. However, the spacing of the observation sites is insufficient to explore such thin structures. Additional MT measurements at a closer spacing are required to image the subsurface structures surrounding the linear clusters of earthquake swarms beneath Hakone volcano.

Additional file

Additional file 1. Epicentral distributions of swarm activities in 2001, 2009, 2011, 2013 and 2015; and vertical cross sections of the obtained resistivity structure overlain by the hypocentres of such swarm epochs.

Abbreviations

AMT: audio-frequency magnetotelluric; WMT: wideband magnetotelluric; ASL: above sea level; SL: sea level; BSL: below sea level; RMS: root-mean-square.

Authors' contributions

RY led the AMT acquisition, data analysis, inversions and discussions for this study. YO was responsible for the WMT survey. YO, YY, WK, SK, HH, TG, RH, MH, TY, MK, SK, TH, TS, YY and MT participated in the field work. YU assisted in the inversions. All authors contributed to preparation of the manuscript. All authors read and approved the final manuscript.

Author details

[1] Disaster Prevention Research Institute, Kyoto University, Gokasyo, Uji, Kyoto 611-0011, Japan. [2] Volcanic Fluid Research Center, Tokyo Institute of Technology, Ookayama 2-12-2, Meguro-ku, Tokyo 152-8551, Japan. [3] Hot Springs Research Institute of Kanagawa Prefectural Government, Iriuda 586, Odawara, Kanagawa 250-0031, Japan. [4] Aso Volcanological Laboratory, Institute for Geothermal Sciences, Graduate School of Science, Kyoto University, Kumamoto 869-1404, Japan. [5] Geological Survey of Japan, National Institute of Advanced Industrial Science and Technology, Tsukuba 305-8567, Japan. [6] Present Address: Geothermal Energy Research & Development Co., Ltd., Tokyo 104-0033, Japan. [7] Graduate School of Engineering, Kyoto University, Kyoto 615-8540, Japan. [8] Graduate School of Science, Kyoto University, Kyoto 611-0011, Japan. [9] Graduate School of Engineering, Tottori University, Tottori 698-8552, Japan.

Acknowledgements
We thank the landowners who kindly provided access to their properties during the AMT surveys, as well as the national, prefectural, city and town offices for their support. The WMT data used in this work were obtained as part of the integrated research project for the Kannawa-Kozu-Matsuda fault zone, which was supported by the Ministry of Education, Culture, Sports, Science and Technology (MEXT) of Japan. We are grateful to Kazutaka Mannen for valuable comments on buried structures and the geology of Hakone caldera. Valuable comments from two anonymous reviewers helped to improve the manuscript. We thank the Disaster Prevention Research Institute, Kyoto University, and the Tokyo Institute of Technology for lending the MT equipment used in the AMT surveys. Most of the figures were prepared with the Generic Mapping Tools software (Wessel and Smith 1998).

Competing interests
The authors declare that they have no competing interests.

Availability of data and materials
The data that support the findings of this study are available upon request from the corresponding author.

Consent for publication
Not applicable.

Ethics approval and consent to participate
Not applicable.

Funding
This study was partially funded by the Disaster Prevention Research Institute, Kyoto University.

Publisher's Note

Received: 29 December 2017 Accepted: 19 April 2018
Published online: 26 April 2018

References

Avdeeva A, Moorkamp M, Avdeev D, Jegen M, Miensopust M (2015) Three-dimensional inversion of magnetotelluric impedance tensor data and full distortion matrix. Geophys J Int 202:464–481. https://doi.org/10.1093/gji/ggv144

Gamble TD, Goubau WM, Clarke J (1979) Magnetotellurics with a remote magnetic reference. Geophysics 44:53–67. https://doi.org/10.1190/1.1440923

Gasperikova E, Rosenkjaer GK, Arnason K, Newman GA, Lindsey NJ (2015) Resistivity characterization of the Krafla and Hengill geothermal fields through 3D MT inverse modeling. Geothermics 57:246–257. https://doi.org/10.1016/j.geothermics.2015.06.015

Hirano T, Yokoyama T, Oki Y, Matsuo S, Watanabe S, Yanagiuchi S (1982) Chemical composition, hydrogen and oxygen isotope ratios for waters of Lake Ashi and groundwaters of the lake-side (in Japanese with English abstract). Bull Hot Springs Res Inst Kanagawa Prefect 13(5):55–64

Kanda W, Tanaka Y, Utsugi M, Takakura S, Hashimoto T, Inoue H (2008) A preparation zone for volcanic explosions beneath Naka-dake crater, Aso volcano, as inferred from magnetotelluric surveys. J Volcanol Geoth Res 178:32–45. https://doi.org/10.1016/j.jvolgeores.2008.01.022

Kisimoto K (2000) Combined bathymetric and topographic mesh data: Japan250 m.grd. Geological Survey of Japan Open-file Report #353

Komori S, Kagiyama T, Utsugi M, Inoue H, Azuhata I (2013) Two-dimensional resistivity structure of Unzen Volcano revealed by AMT and MT surveys. Earth Planets Space 65:759–766. https://doi.org/10.5047/eps.2012.10.005

Mannen K (2014) Post-caldera geology of Gora region in Hakone volcano group, Japan (in Japanese with English abstract and captions). J Geol Soc Jpn 120(4):117–136. https://doi.org/10.5575/geosoc.2014.0007

Nurhasan et al (2006) Two electrical conductors beneath Kusatsu-Shirane volcano, Japan, imaged by audiomagnetotellurics, and their implications for the hydrothermal system. Earth Planets Space 58:1053–1059. https://doi.org/10.1186/BF03352610

Ogawa Y, Kanda W, Yoshimura R, Uyeshima M (2011) Magnetotelluric survey around the western end of the Kannawa fault. In: Report of the integrated research project for Kannawa-Kozu-Matsuda fault zone (in Japanese). http://jishin.go.jp/main/chousakenkyuu/kannawa_juten/h23/chap3_1_d.pdf. Accessed 1 Dec 2017

Ohba T, Daita Y, Sawa T, Taira N, Kakuage Y (2011) Coseismic changes in the chemical composition of volcanic gases from the Owakudani geothermal area on Hakone volcano, Japan. Bull Volc 73:457–469. https://doi.org/10.1007/s00445-010-0445-9

Pellerin L, Johnston JM, Hohmann GW (1996) A numerical evaluation of electromagnetic methods in geothermal exploration. Geophysics 61(1):121–130. https://doi.org/10.1190/1.1443931

Sasaki Y, Meju MA (2006) Three-dimensional joint inversion for magnetotelluric resistivity and static shift distributions in complex media. J Geophys Res 111:B05101. https://doi.org/10.1029/2005jb004009

Schwalenberg K, Rath V, Haak V (2002) Sensitivity studies applied to a two-dimensional resistivity model from the Central Andes. Geophys J Int 150:673–686. https://doi.org/10.1046/j.1365-246X.2002.01734.x

Seki K, Kanda W, Ogawa Y, Tanbo T, Kobayashi T, Hino Y, Hase H (2015) Imaging the hydrothermal system beneath the Jigokudani valley, Tateyama volcano, Japan: implications for structures controlling repeated phreatic eruptions from an audio-frequency magnetotelluric survey. Earth Planets Space 67:6. https://doi.org/10.1186/s40623-014-0169-8

Seki K et al (2016) Resistivity structure and geochemistry of the Jigokudani Valley hydrothermal system, Mt. Tateyama, Japan. J Volcanol Geoth Res 325:15–26. https://doi.org/10.1016/j.jvolgeores.2016.06.010

Si H (2015) TetGen, a Delaunay-Based quality tetrahedral mesh generator. ACM Trans Math Softw 41(2):11. https://doi.org/10.1145/2629697

Szarka T, Menvielle M (1997) Analysis of rotational invariants of the magnetotelluric impedance tensor. Geophys J Int 129:133–142. https://doi.org/10.1111/j.1365-246X.1997.tb00942.x

Ussher G, Harvey C, Johnstone R, Anderson E (2000) Understanding the resistivities observed in geothermal systems. Proc World Geotherm Cong 2000:1915–1920

Usui Y (2015) 3-D inversion of magnetotelluric data using unstructured tetrahedral elements: applicability to data affected by topography. Geophys J Int 202:828–849. https://doi.org/10.1093/gji/ggv186

Usui Y et al (2017) Three-dimensional resistivity structure of Asama Volcano revealed by data-space magnetotelluric inversion using unstructured tetrahedral elements. Geophys J Int 208:1359–1372. https://doi.org/10.1093/gji/ggw459

Wessel P, Smith WHF (1998) New, improved version of Generic Mapping Tools released. EOS Trans AGU 79(47):579. https://doi.org/10.1029/98EO00426

Yamaya Y et al (2013) A large hydrothermal reservoir beneath Taal Volcano (Philippines) revealed by magnetotelluric resistivity survey: 2D resistivity modeling. Bull Volc 75:729. https://doi.org/10.1007/s00445-013-0729-y

Yoshimura R et al (2012) AMT observations over the seismic active region in Hakone volcano -preliminary results (in Japanese with English abstract and captions). Ann Disaster Prev Res Inst 55B:105–111

Yoshimura R et al (2013) Complementary AMT observations around the 2013 swarm activity in Hakone volcano (in Japanese with English abstract and captions). Ann Disaster Prev Res Inst 56B:153–156

Yukutake Y, Tanada T, Honda R, Harada M, Ito H, Yoshida A (2010) Fine fracture structures in the geothermal region of Hakone volcano, revealed by well-resolved earthquake hypocenters and focal mechanisms. Tectonophysics 489:104–118. https://doi.org/10.1016/j.tecto.2010.04.012

Yukutake Y, Ito H, Honda R, Harada M, Tanada T, Yoshida A (2011) Fluid-induced swarm earthquake sequence revealed by precisely determined hypocenters and focal mechanisms in the 2009 activity at Hakone volcano, Japan. J Geophys Res 116:B04308. https://doi.org/10.1029/2010JB008036

Yukutake Y et al (2013) Remotely triggered seismic activity in Hakone volcano during and after the passage of surface waves from the 2011 M9.0 Tohoku-Oki earthquake. Earth Planet Sci Lett 373:205–216. https://doi.org/10.1016/j.epsl.2013.05.004

Yukutake Y, Honda R, Harada M, Arai R, Matsubara M (2015) A magma-hydrothermal system beneath Hakone volcano, central Japan, revealed by highly resolved velocity structures. J Geophys Res 120:3293–3308. https://doi.org/10.1002/2014JB011856

Yukutake Y et al (2017) Analyzing the continuous volcanic tremors detected during the 2015 phreatic eruption of the Hakone volcano. Earth Planets Space 69:164. https://doi.org/10.1186/s40623-017-0751-y